12

Interaction Region and Backgrounds

The PEP-II requirements of high beam currents, asymmetric energies, and head-on collisions conspire to make machine-induced backgrounds a significant challenge in the design of PEP-II and the *BaBar* detector. To achieve head-on collisions with asymmetric energies and 1.26 m bunch spacing, beam line elements must be positioned very close to the interaction point. The detector must be well protected from excessive occupancies and radiation damage, while maintaining a large solid-angle acceptance for $\Upsilon(4S)$ decays. The expected sources of detector backgrounds are:

- synchrotron radiation photons produced in the machine magnetic elements;
- lost beam particles (bremsstrahlung and Coulomb scattering off residual gas molecules);
- luminosity-related backgrounds such as elastic and radiative Bhabha scattering; and
- other sources such as inelastic beam-gas interactions, cosmics, muons from collimators, etc.

These background sources can give rise to primary particles that either enter the detector directly or generate secondary debris that ultimately reaches the detector.

This chapter describes the various background sources and the results of simulations aimed at estimating the rates and impacts on the various detector components. Section 12.1 describes the interaction region design and the effect of background considerations on that design. Also in this section is a discussion of PEP-II operating modes, including issues relating to injection. Sections 12.2 and 12.3 describe the tools used to study the above backgrounds and estimates rates for each. Section 12.4 describes in detail the effect of the backgrounds on each of the major detector components in *BaBar*.

Parameter	HER	LER	Units
Center-of-Mass Energy	10.580		GeV
Peak Luminosity	3.0×10^{33}		$cm^{-2}s^{-1}$
Luminosity Lifetime	1.55		hr
Bunch Spacing	1.26		m
Circumference	2219.3		m
Beam Energy	9.000	3.109	GeV
Bunch Length	1.0	1.0	cm
Number of Bunches	1658	1658	
Particles per Bunch	2.73×10^{10}	5.91×10^{10}	
Beam Current	0.986	2.140	Amps
Transverse Damping Time	36.8	54.0	msec
Horizontal Emittance	48.2	64.3	nm-rad
Horizontal IP Beta	50.0	37.5	cm
Horizontal IP Spot Size	155	155	μm
Horizontal Tune Shift	0.03	0.03	
Vertical Emittance	1.93	2.57	nm-rad
Vertical IP Beta	2.00	1.50	cm
Vertical IP Spot Size	6.2	6.2	μm
Vertical Tune Shift	0.03	0.03	

Table 12-1. *PEP-II parameters.*

12.1 PEP-II Design

12.1.1 Parameters

The PEP-II project is an e^+e^- colliding beam storage ring complex designed to produce a luminosity of at least $3 \times 10^{33}\,\mathrm{cm}^{-2}\mathrm{s}^{-1}$ at $E_{cm} = 10.58\,\mathrm{GeV}$, equivalent to the mass of the $\Upsilon(4S)$ resonance, with unequal energy beams of 3.1 and 9.0 GeV. The parameters of the accelerator are listed in Table 12-1. Both the high luminosity and the energy asymmetry require significant advances in storage ring design and construction. A full description of the PEP-II project may be found in the PEP-II Conceptual Design Report [PEP93].

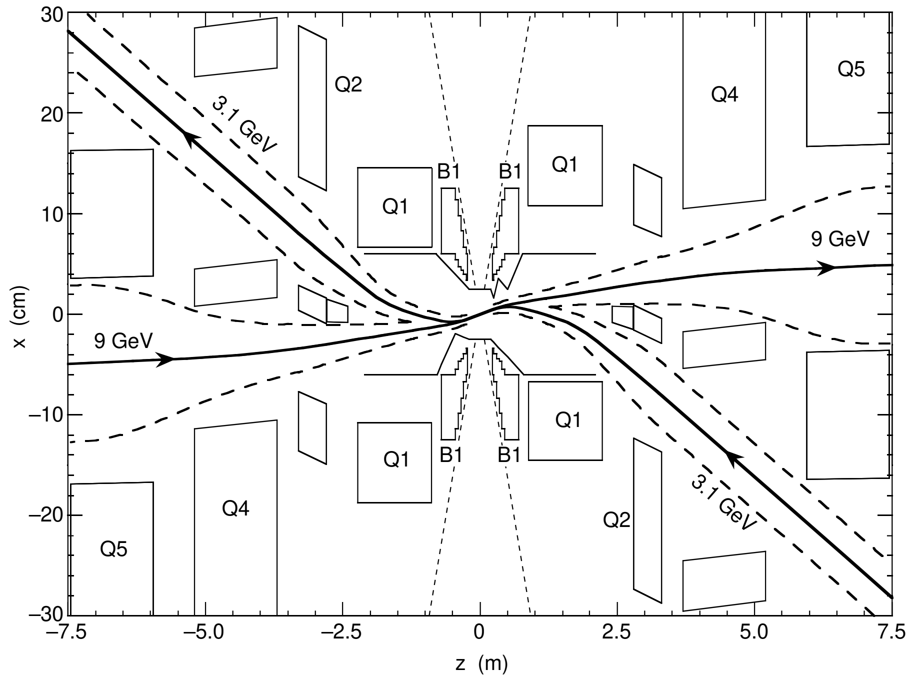

Figure 12-1. *Plan view of the interaction region. The low-energy beam enters from the lower right and exits from the upper left. The high-energy beam enters from the left and exits on the right. The vertical scale is highly exaggerated. The dashed lines represent the beam stay-clear envelopes, and the 300 mr detector acceptance cutoff.*

12.1.2 Interaction Region Components

The high luminosity of PEP-II is achieved through high beam currents and strong focusing. The high current must be divided into a large number of low-charge bunches to avoid the beam-beam tune-shift limit, and the beams must collide only at the IP to avoid additional tune shift. PEP-II collides the beams head on but separates the beams horizontally before the next collision at 62 cm from the interaction point (IP), utilizing the energy asymmetry and separation dipoles (B1) within 20 cm of the IP. Strong focusing requires quadrupoles located close to the IP. The final quadrupole Q1 is common to both beams and starts at 90 cm from the IP, partially penetrating the central detector. The low-energy beam (LEB) is off-axis in Q1 to maximize the beam separation. The next quadrupole Q2 focuses only the LEB, with the high-energy beam (HEB) passing through a field-free region. The following pair of quadrupoles, Q4 and Q5, focus only the HEB, with the LEB passing through a field-free region. The layout of the PEP-II interaction region is shown in Figure 12-1. It is described in more detail in the PEP-II Conceptual Design Report [PEP93, pages 55–58 and 66–74].

The B1 and Q1 magnets are inside the 1.5 T detector solenoid field. Conventional iron magnets do not function in this environment, so the only possibilities are superconducting and permanent magnets. There is not enough room between the beam pipe and the 300 mr detector acceptance envelope at the location of B1 to allow a cryostat, so the only option is a permanent magnet. In the PEP-II baseline design, Q1 is also a permanent magnet. (A superconducting Q1 design is presently under consideration. It would not change the IR optics in a fundamental way, nor would it change the luminosity, but it would allow greater operational flexibility at a significantly higher cost.)

B1 and Q1 are constructed of rings of SmCo permanent magnet material. Each ring is constructed of blocks with their magnetic moments normal to the beam direction and varying in azimuth around the beam in the manner described by Halbach [Hal81]. Permanent quadrupole magnets very similar to Q1 have been used at the Cornell Electron Storage Ring for many years [Her87a, Her87b].

The beam pipe at the interaction point is a double-wall structure, with an inner tube 50 mm in diameter and 800 μm thick, separated by 2 mm from an outer tube of 400 μm thickness, with helium gas flowing between the tubes for cooling. It is made of beryllium to minimize multiple scattering but is coated inside with 10 microns of gold to attenuate synchrotron radiation, totaling 0.6% of a radiation length. (The background studies have primarily assumed 25 μm of copper rather than 10 μm of gold.)

There are water-cooled masks inside the B1 magnet to prevent synchrotron radiation from striking the beam pipe. There are additional masks to protect the septum region of the Q2 quads from synchrotron radiation. The IP beam pipe and synchrotron radiation masks are described in the PEP-II Conceptual Design Report [PEP93, pages 357–371].

The two Q1 magnets, two B1 magnets, IP beam pipe, and vertex detector are assembled into a single rigid support barrel of 43 cm outside diameter, shown in Figure 12-2. The designs for B1, Q1, Q2, and the support tube are described in Reference [PEP93, pages 276–301].

The support barrel is assembled and internally aligned outside the detector and installed by sliding it through the drift chamber. The two end sections of the support barrel are made from stainless steel and carry the Q1 magnet assemblies. The middle barrel section is a carbon-fiber composite equivalent to $0.005X_0$ in thickness. The total assembled weight is approximately 2500 kg, concentrated in the end sections.

12.1.3 Background Implications

The bending near the IP required to separate the beams generates a large synchrotron radiation flux that is not present in more conventional e^+e^- colliders. The bending also sweeps off-energy beam particles into the detector. There are also many more bunch crossings

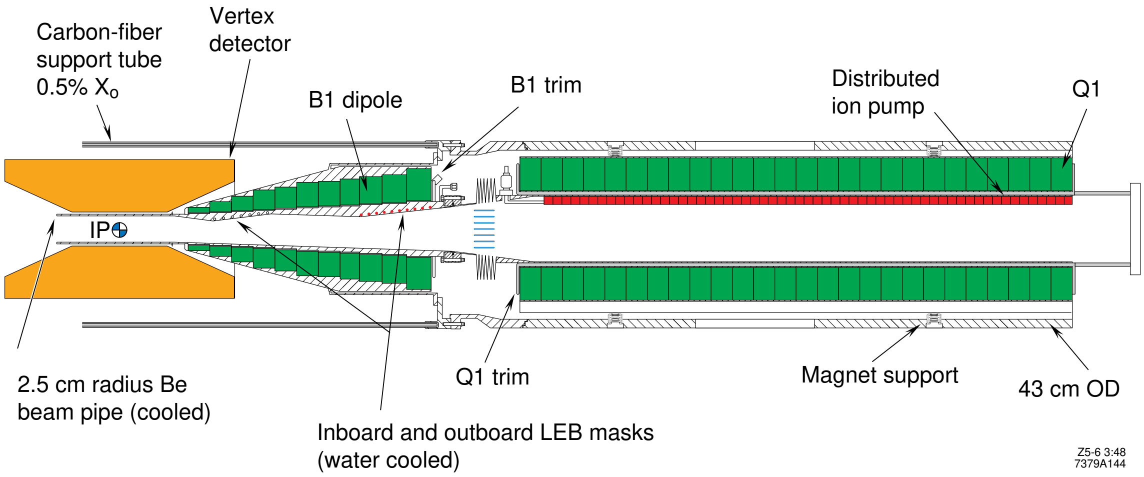

Figure 12-2. *Support barrel for interaction-region components inside the detector. Only one end is shown.*

within the detector resolving time than in previous colliders. Machine-induced detector backgrounds have been considered in the PEP-II design optimization process from the start. The synchrotron radiation and lost-particle backgrounds have been calculated during the accelerator design iteration process, and the design has been altered to minimize the backgrounds. For example, the Q4 quadrupole is offset from the HEB orbit so that synchrotron radiation from Q5 that would otherwise hit the IP beam pipe is directed into a mask.

The B1 magnets have a dipole field of 0.75 T and produce an intense synchrotron radiation fan, but it is generated so close to the IP that most of it travels harmlessly through the beam pipe and is absorbed far away. Masks have been designed to prevent other sources of synchrotron radiation from shining directly onto the IP beam pipe. The B1 and offset Q1 magnets bend in opposite directions and are on opposite sides of the IP, which allows the masks to be on only one side of the beam pipe minimizing backscattering problems. The synchrotron radiation from the LEB has a low critical energy, so it is easily absorbed by the copper beam pipe. The physical aperture of the machine vacuum chamber has been designed to increase relative to the local beam size when traveling from the machine arcs to the IP. Adjustable beam collimators will absorb distant and local beam-gas bremsstrahlung and Coulomb scattering. Special attention has been paid to the vacuum system near the IP to minimize beam-gas scattering. The B1 and Q1 magnets serve as effective shielding for lost particles.

12.1.4 Operating Modes

Most background calculations are based on stable colliding beams. The dominant beam loss mechanism is then beam-gas scattering distributed around the rings, although beam-beam bremsstrahlung at the IP can become comparable at high luminosity. The high dispersion in the bending arcs prevents damaging products of distant beam-gas bremsstrahlung from reaching the detector. Beam-gas bremsstrahlung in the upstream part of the IR straight section is stopped by collimators, but bremsstrahlung close to the detector produces irreducible backgrounds. Beam-gas coulomb scattering far from the detector is also absorbed by collimators and in general is less of a problem than bremsstrahlung. Most synchrotron radiation is directed away from the detector, and the remaining radiation is largely absorbed by masks. There is an irreducible background from scattering off the tips of the masks.

On the order of once per hour, it will be necessary to inject into PEP-II. The injection process and components are described in Reference [PEP93, pages 483–560]. Normal injection will be in top-off mode, *i.e.,* charge will be injected without dumping the stored beam. This mode and re-injecting after a total beam loss are projected to require on the order of six minutes to complete. The beams will be injected at collision energy into collision optics, with no necessity to ramp or squeeze the beams. The beam emittance provided by the injector (the Stanford Linear Collider with some modifications) will be smaller than the equilibrium emittance of PEP-II. Therefore, injection will be possible with all collimators at the settings assumed for background calculations.

A beam particle damps from its injected orbit to the stored orbit in a small fraction of a second, compared to the expected lifetime of many thousands of seconds. Thus, any radiation dose from the capture process is expected to be much less important than radiation from the normal stored condition. There is no known reason for the injection process not to be highly efficient, or for injection losses to produce larger detector radiation doses than losses from the stored beam. Since injection will take place when a few tens of percent of the stored beam has been lost, the dose from injection will not dominate unless the injection inefficiency is worse than tens of percent. There is a sufficient safety margin in the radiation damage thresholds that, if injection resulted in a dose comparable to normal running, this would be acceptable.

Signals from the detector or local radiation monitors will be used as inputs to the PEP-II beam-dumping system. If a rapid increase in radiation is observed, the stored beam will be dumped into a distant absorber. Such systems are in use already by the LEP detectors. The injection process will also be interrupted if radiation is observed to be abnormally high. It is assumed that particularly sensitive detector components like the drift chamber will be ramped down during injection to minimize radiation damage, and injection will be dependent on these components being ready.

12.2 Tools

12.2.1 QSRAD

The program QSRAD was built to study synchrotron radiation generated by the beam as it traveled through the last two focusing magnets prior to the collision point in PEP-I. The program traces weighted rays from a Gaussian beam profile through the specified magnetic optics and produces a geometric fan of synchrotron radiation with equal power density and constant critical energy for each magnetic element. These fans are then traced, and a tally is made of the fraction of each fan that strikes defined apertures. Apertures are specified in planes transverse to the beam. An aperture can be a circle, an ellipse, a horizontal slit, or a vertical slit. The distribution of photon critical energies is accumulated for each aperture and converted to a photon energy distribution. In addition, the beam rays that strike each aperture are recorded, and a table of x, y locations is produced, indicating the origin in the beam profile for those particles.

An enhanced version of QSRAD (called SYNC_BKG) is used to calculate B Factory synchrotron radiation rates. The following improvements to SYNC_BKG have been implemented: a non-Gaussian beam tail distribution can be added to the beam profile. The beam tail distribution is modeled as a lower flatter Gaussian beam profile; tilted and offset quadrupoles are allowed; horizontal and vertical bend magnets are recognized as magnetic elements; and individual magnetic elements can be subdivided to more accurately simulate long quadrupoles.

The information from SYNC_BKG on photon rates striking various surfaces near the IP is used in a second stage to study backscattering and tip scattering from the mask surfaces. EGS4 [Nel85] (which includes Rayleigh scattering and K-shell fluorescence) is used to calculate the number and energy of photons that scatter from a mask tip, penetrate the detector beam pipe, and are absorbed in various layers of the silicon vertex detector.

12.2.2 Decay TURTLE

Decay TURTLE [Car91] is a program for tracking particles and decay secondaries through beam line components. A version of this package has been modified to do bremsstrahlung and Coulomb scattering. A scattering point is picked randomly along the beam line, a beam particle transported to that point, and the scattered secondary propagated down the remaining beam line until it hits an aperture or the end of the beam line. For bremsstrahlung scattering the photon is also propagated. Scoring planes are used to simulate collimators, masks, and other apertures. Selected particles, particularly ones hitting an aperture near the IP, can be written to a disk file for later input to the GEANT or OBJEGS detector simulations described below.

In the studies presented here, the PEP-II machine lattice is simulated from the middle of the preceding arc to several meters downstream of the IP ($\sim$185 m). Placement of collimators in the interaction region reduces the rate of upstream scatters reaching the IP. A graded aperture is employed in this region of the machine lattice ($\pm$60 m from the IP), *i.e.,* progressively larger apertures are used as one approaches the IP. Multiturn effects have not yet been studied. Optimization and design of upstream collimation is in progress subject to space constraints and the avoidance of significant synchrotron power dissipation on the collimator.

12.2.3 OBJEGS

OBJEGS [Hea91] interfaces EGS4 [Nel85] to simple cylindrical geometries. The user specifies beam line and detector components in terms of the inner and outer radius, lower and upper longitudinal limits, and material type. Files of lost particles from TURTLE or other sources of background such as radiative Bhabhas can be input from a file one particle at a time. Integration over time must be done as a separate step operating on the output of OBJEGS. This can be as simple as adding up total energy deposits to obtain the radiation dose or as complex as combining hits produced by multiple rays to make events for a trigger simulation.

The restriction to cylindrical geometries in OBJEGS makes it impossible to describe the *BaBar* detector perfectly, especially as the detector design has grown more sophisticated and realistic with features such as conical drift chamber end plates and variable crystal lengths. The biggest problem for OBJEGS geometries is the elliptical shape of the synchrotron radiation mask; to approximate this, two versions of OBJEGS geometries are used—one that reproduces the longitudinal profile of the low-energy beam synchrotron mask, and one that reproduces the high-energy synchrotron mask. The geometry corresponding to the side of the detector which is struck by a particle is used for the simulation of the shower produced by that particle. Due to these complications, *BaBar* has been moving toward a GEANT-based simulation (Section 12.2.4) as its primary detector simulation tool. A number of the studies in this document were performed using OBJEGS, but will be redone with GEANT as time permits.

12.2.4 GEANT

An extensive GEANT [GEA94] simulation of the *BaBar* detector, called BBSIM, is currently the primary tool for detector performance studies. As part of this implementation, there is

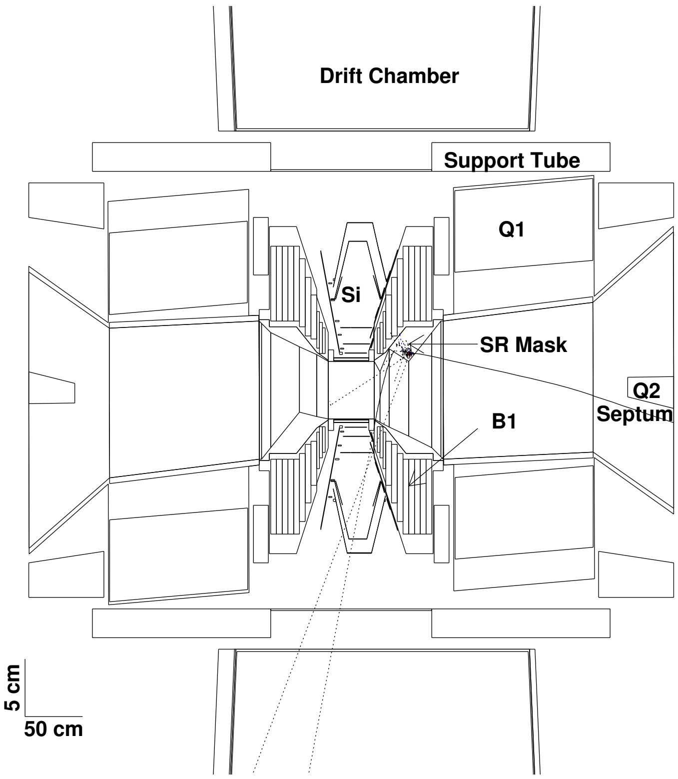

Figure 12-3. *GEANT simulation of beam line components. The interaction of a LEB lost beam particle is also shown (with a high shower cut-off energy of 10 MeV).*

a rather detailed simulation of the beam line components. Figure 12-3 shows an expanded view of this central part of the *BaBar* detector with a lost beam particle generated with the TURTLE package described above.

The simulation includes an approximation to the synchrotron radiation masks, which have an elliptical aperture, and the B1 and Q1 beam line magnet elements. The dipole and quadrupole fields of the B1 and Q1 (both SmCo permanent magnets), respectively, are also included. At the ends of the beam pipe are the Q2 septum masks that shield the Q2 coil.

Files of lost particles or radiative Bhabhas can be input to the simulation, either one particle scatter at a time or integrated over some detector time window and superimposed on a physics event.

12.2.5 GELHAD

GELHAD [Sny94] is a program for simulating the electro-production of hadrons via γN interactions. The interactions of electrons with nuclei can be added using a virtual photon approximation; however, hadronic interactions in electromagnetic showers are dominated by real γN interactions.

GELHAD is based on subroutines from the hadronic shower simulation GHEISHA [Fes85]. Two basic models are available: (1) the photon is absorbed by one nucleon that is then forced to interact with the residual nucleus; and (2) the photon is replaced by a pion of the same energy that interacts with the nucleus. In both models, energy conservation and charge conservation are respected, but in general, momentum conservation is violated. The default used in most of the studies for this document uses model (1) below $E_\gamma = 150\,\mathrm{MeV}$ and model (2) above.

GELHAD has been implemented both in OBJEGS and GEANT. Trigger studies with the OBJEGS version use the supplementary program TRACK [Sny94] to simulate the behavior of hadrons in OBJEGS geometries. GEANT-based studies have, of course, the full power of GEANT and the detailed BBSIM geometry available.

12.3 Background Sources

12.3.1 Synchrotron Radiation

There are several sources of synchrotron radiation backgrounds:

- direct synchrotron radiation;
- photons that scatter off a mask tip;
- synchrotron radiation from elements far upstream of the interaction point; and
- sources of backscattered photons from downstream surfaces.

Separating the unequal-energy beams by the use of bending magnets and offset quadrupoles generates several fans of synchrotron radiation. The geometry of the interaction region optics, however, is designed to minimize the amount of synchrotron radiation that strikes nearby surfaces. In particular, the S-bend geometry of the beam lines allows most of the synchrotron radiation generated by magnetic elements upstream of the interaction region to pass through the detector region without hitting local surfaces. Primary masks near the collision point are used to prevent direct radiation from hitting the detector beam pipe, while at the same time keeping the number of photons that strike the mask tips to an acceptable level. The synchrotron radiation fans from both beams are shown in Figure 12-4.

The LEB generates synchrotron radiation fans as it passes through the Q1 and B1 magnets on its way to the collision point. The LEB mask is designed to prevent the synchrotron radiation (either fan or quadrupole) generated by the upstream magnets from directly striking the detector beam pipe. The surfaces of the LEB mask are sloped such that scattered photons cannot travel directly to the detector beam pipe. The LEB mask absorbs about 3.6 kW of synchrotron radiation power. Fans generated by the LEB in the two B1 magnets and in the downstream Q1 magnet pass through the interaction region without striking nearby surfaces. The first surface that intercepts the B1 fans is the septum mask in front of the Q2 septum quadrupole, located 2.8 m from the IP. This septum mask absorbs 3.5 kW of power.

Synchrotron radiation fans generated by the HEB in upstream bend magnets and offset quadrupole magnets deposit nearly 1 kW of power on the HEB mask. These upstream HEB elements are positioned to ensure that radiation generated by beam particles even 10σ off-axis in these elements does not strike the LEB mask. The fans of radiation generated by the HEB as it passes through the two B1 magnets do not strike any surfaces in the detector region and are absorbed in a dump about 17 m downstream of the detector.

The geometry of the masking near the IP is such that no synchrotron radiation can hit the IP beam pipe directly, nor can it scatter off the face of a mask onto the IP beam pipe. Scattering from the tips of the LEB and HEB masks is the dominant source of photons striking the detector beam pipe. This process has been simulated in great detail. The individual photons that strike the LEB and HEB mask tips are generated from an energy spectrum given by a program that traces the photons from sources to surfaces of interest. The photons that end up striking the detector beam pipe are followed through the detector components by the EGS Monte Carlo program [Nel85]. Further details of this simulation package can be found in Reference [PEP93, pages 108–112]. The results of the simulations are the photon spectra shown in Figure 12-5; backgrounds resulting from synchrotron radiation are shown in Table 12-2.

Other sources of synchrotron radiation, such as magnets farther upstream, and backscatter from the Q2 septum masks, produce negligible contributions to the detector background compared to primary mask tip scattering. While a high photon flux strikes the dump for HEB radiation from the B1 magnets, the small solid angle of the detector beam pipe as seen from this source, the photon's small angle of incidence on the beam pipe, and the fact that most of the beam pipe is shielded by the LEB mask, together reduce the background from the 17 m dump to a low level.

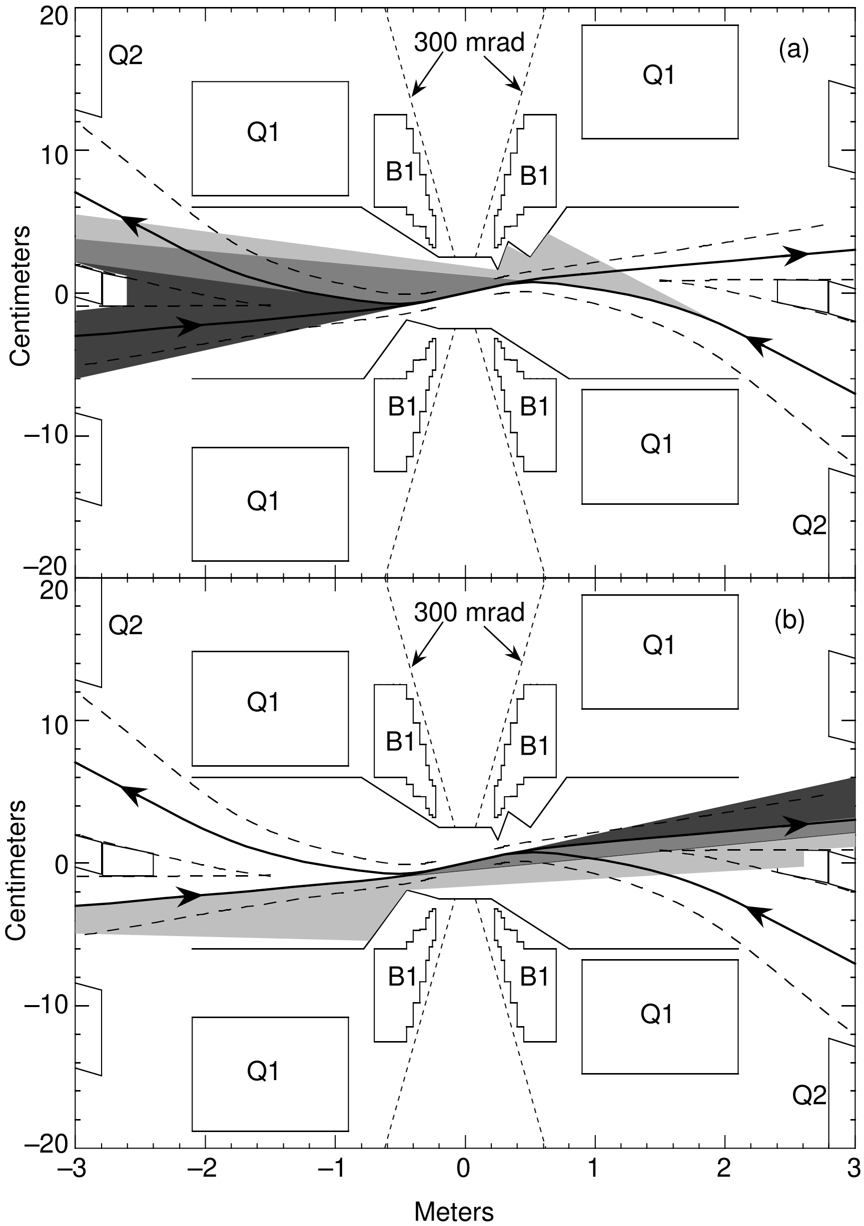

Figure 12-4. *Synchrotron radiation fans from the low-energy (a) and high-energy (b) beams. The density of shading gives an indication of the relative photon intensity from the various radiation fans.*

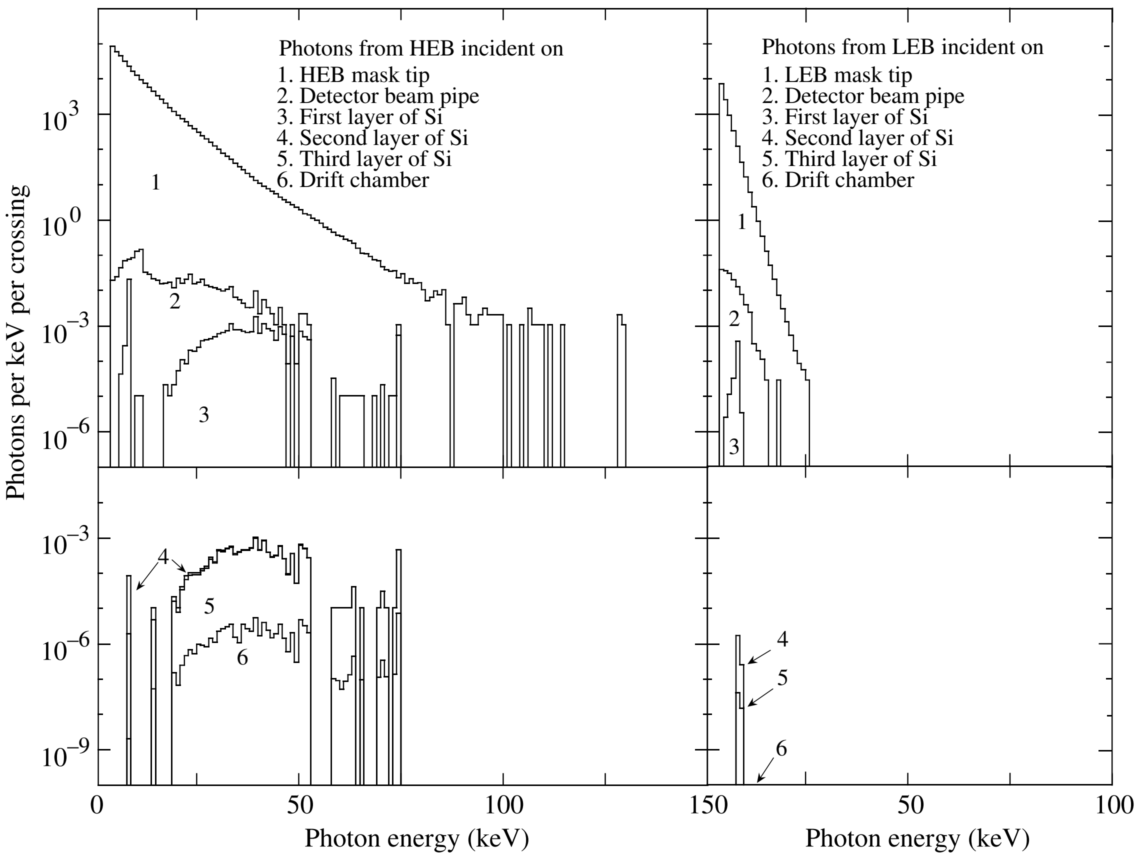

Figure 12-5. *Photon spectra from synchrotron radiation. Left plot is for high-energy beam; right plot is for low-energy beam.*

The effect of magnet misalignments on detector backgrounds has also been evaluated. Of the 24 different cases studied, two cases, a ± 5 mm displacement in x of Q1, Q4, and Q5, produced a threefold increase in the background rate. The rest of the misalignment checks produced small ($< 50\%$) increases in backgrounds, with some configurations producing rates that are actually below the nominal background rate. None of these misalignment checks resulted in synchrotron radiation photons directly striking the detector beam pipe.

12.3.2 Lost Particles

Bremsstrahlung and Coulomb scattering of beam particles from residual gas molecules in the beam pipe can result in high-energy beam particles and photons striking masks and the beam pipe near the IP. The resulting electromagnetic showers can cause excessive detector

	Incident on Be Pipe	Absorbed in First Si Layer	Absorbed in Second Si Layer	Absorbed in Third Si Layer	Incident on Drift Chamber
$4 < E_\gamma < 100\,\mathrm{keV}$					
# of Photons	1.24	0.028	6.9×10^{-4}	5.6×10^{-4}	2.4×10^{-5}
Energy (keV)	17.6	0.43	2.2×10^{-2}	2.0×10^{-2}	3.2×10^{-3}
$4 < E_\gamma < 20\,\mathrm{keV}$					
# of Photons	0.96	0.022	3.8×10^{-5}	8.6×10^{-6}	2.1×10^{-7}
Energy (keV)	9.34	0.17	9.2×10^{-4}	1.3×10^{-4}	3.7×10^{-6}
Detector Limits					
# of Photons	—	2.3	> 2.3	> 2.3	125
Energy (keV)	—	95	> 95	> 95	5000

Table 12-2. *Synchrotron radiation background simulation results. The numbers are for each crossing. Multiply by 238 to get photons per μs. In the simulation, the beam pipe consists of 25 μm of Cu and 1 mm of Be.*

occupancy and/or radiation damage. Hadronic showers from photoproduction can also occur in these showers and are discussed in Section 12.3.3.

Section 12.2.2 describes Decay TURTLE, the tool used to establish the rate of particles incident on the masks and beam pipe near the IP. The rate is reduced significantly with upstream collimation. Recent studies assume a uniform beam line pressure of 1 nTorr (N_2 equivalent) to determine regions of sensitivity to pressure. Additional pumping in these regions can then be employed to further reduce this background. Figure 12-6(a) shows the location of the beam particle scatter for particles that end up striking near the IP. Rates are quoted per μs, a typical integration time for detector elements. Since higher energy particles deposit more energy in the detector, Figure 12-6(b) shows the same distribution weighted with the energy of the scattered particle.

Studies are in progress to determine a realistic estimate of the IR vacuum pressure profile. Preliminary results suggest that, on average, the assumed uniform 1 nTorr distribution is a reasonable baseline for these studies. It appears possible to reach pressures below 1 nTorr (0.2–0.5 nTorr) in the regions from 3 to 40 meters from the IP in both the incoming HEB and LEB beam lines. Due to space constraints at the IP that preclude placement of pumps very close to the IP and the high heat load on the synchrotron radiation masks, the pressure within three meters of the IP will likely exceed 1 nTorr. Scatters very close to the IP (± 1 m) will tend to make it out of the detector region before striking an aperture. Average background rates for these preliminary pressure profiles tend to be comparable to the rates found with the uniform 1 nTorr assumption, so this is taken to be the *nominal* level. Assuming this baseline, the HEB deposits 12.9 GeV per μs from bremsstrahlung scattering and 1.0 GeV

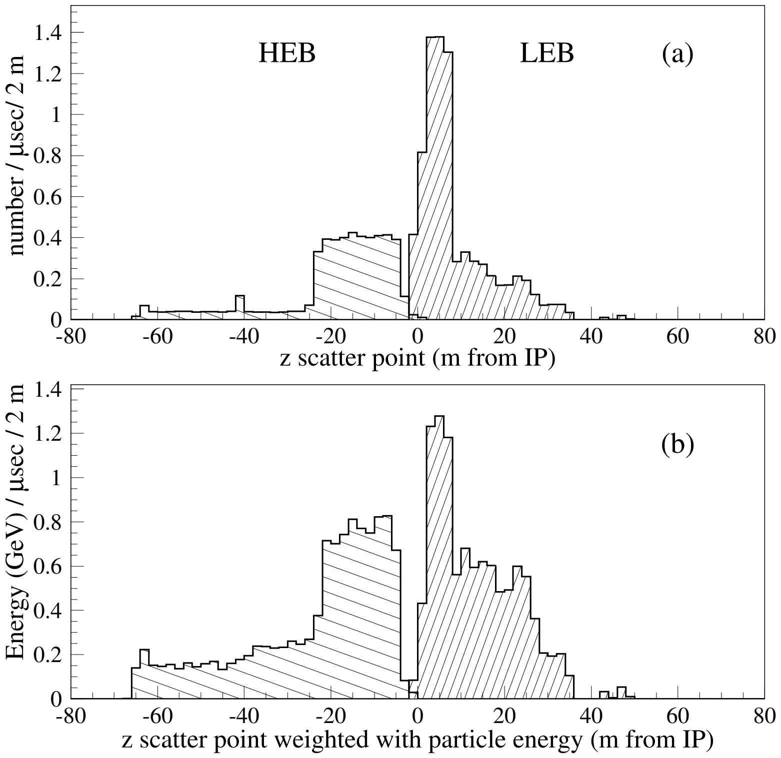

Figure 12-6. *Distribution of the scatter point of beam particles that hit near the IP (a) unweighted and (b) weighted with the energy of the particle. A uniform 1 nTorr vacuum pressure is assumed.*

from Coulomb scattering within ±1.5 m of the IP. The LEB contribution is 9.2 GeV from bremsstrahlung scattering and 1.4 GeV from Coulomb scattering.

GEANT is used in the detector simulation package BBSIM to evaluate the impact of this energy deposition near the IP. Secondaries from electromagnetic showers in the beam line components are followed into the detector elements. The showers are cut off for electron and photon kinetic energies below 50 keV. Figure 12-7 shows the resulting energy, azimuthal, and z distributions for secondary electrons and photons incident on Layer 1 of the silicon vertex detector. The peak at 0.5 GeV in the energy distribution is due to e^+e^- annihilation. The strong peaks in the ϕ distribution at 0° and 180° are from bremsstrahlung scattering in which the B1 dipoles bend the energy-degraded beam particles horizontally into the beam pipe. The other peaks in this distribution are from double counting the flux in regions of overlapping silicon detectors. Figure 12-8 shows the same distributions for Layer 1 of the central drift chamber. Since few photons interact in the drift chamber, the flux into the particle identification system and CsI calorimeter is nearly identical to the flux entering

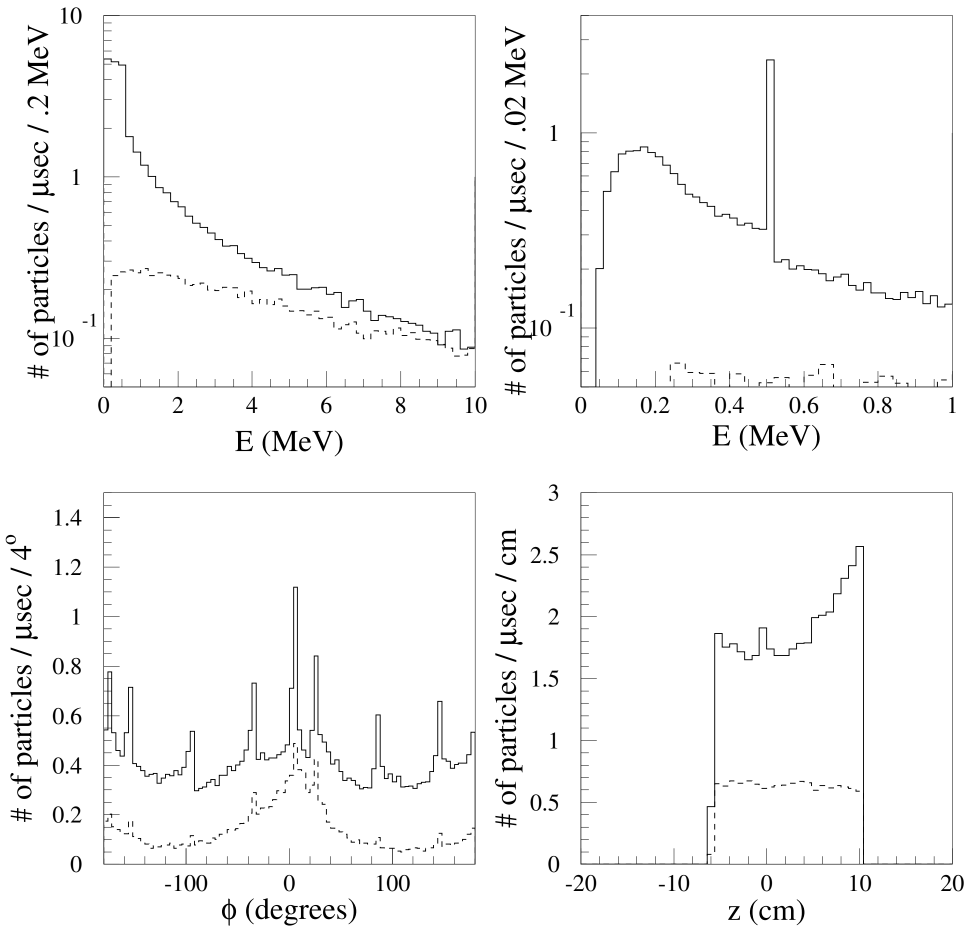

Figure 12-7. *Energy, azimuthal, and z distributions of photons (solid) and electrons (dashed) incident on Layer 1 of the silicon detector for lost beam particle backgrounds. Rates correspond to the number of incident particles per μs.*

the drift chamber. Figure 12-9 shows the distribution for the front face of the calorimeter, including the polar angle distribution of photons and energy flow.

12.3.3 Hadrons

Estimates of trigger rates from photoproduced hadrons are given in Chapter 10. In this section, we seek only to check (using a simplified trigger simulation) whether or not the triggers are produced by photon interactions that could be expected to be well-modeled by GELHAD.

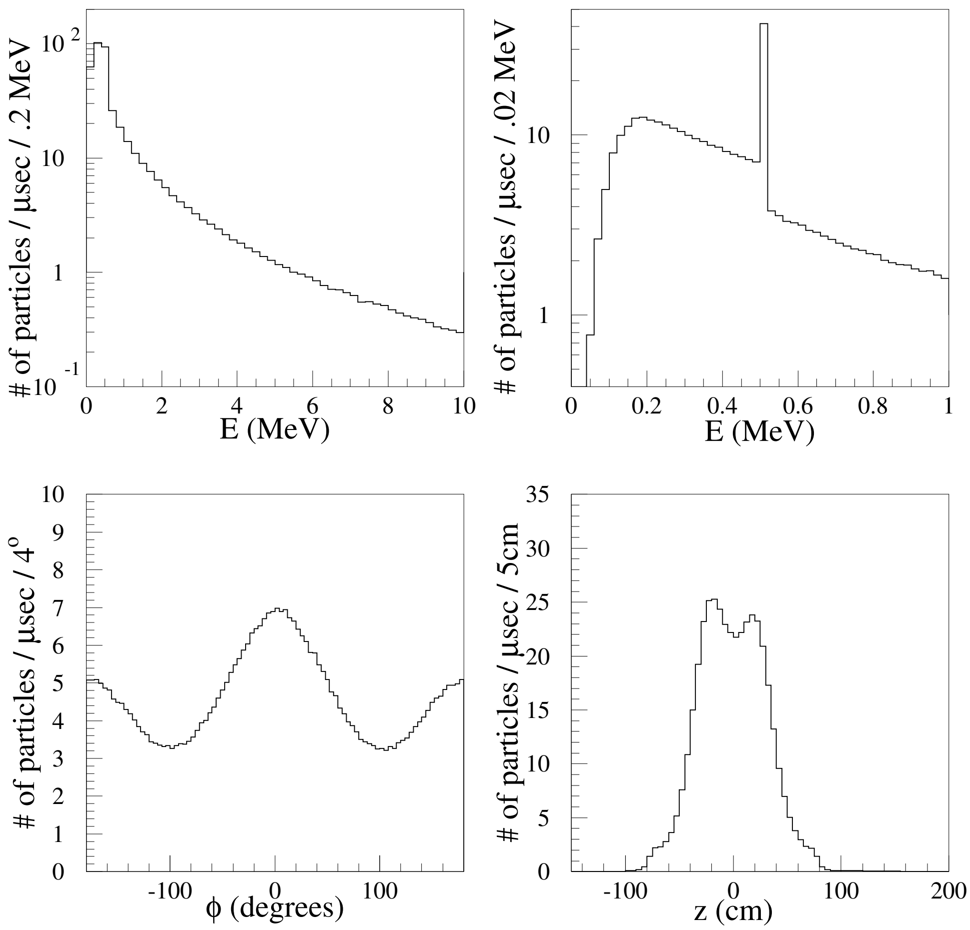

Figure 12-8. *Energy, azimuthal, and z distributions of photons incident on Layer 1 of the central drift chamber for lost beam particle backgrounds. The electron rates are negligible. Rates correspond to the number of incident particles per μs.*

Figure 12-10 shows the distribution of the energy of photons in electromagnetic showers that interact hadronically; only those photons that produced triggers are modeled. The GEANT version of GELHAD has been used to make this distribution. The trigger in this case is a one and one-half track trigger in which at least one track reached the outermost layer of the drift chamber and the other track reached at least the middle layer of the chamber. Note that the spectrum is rather hard, with an average energy of 2400 MeV. This gives us some confidence that our model, which at least conserves charge and energy, may do a reasonable job in the relevant region.

The process of comparing GELHAD with data from the PEGASUS [Deg94] test run using the TPC detector at PEP has just begun and will be vigorously pursued in the next few

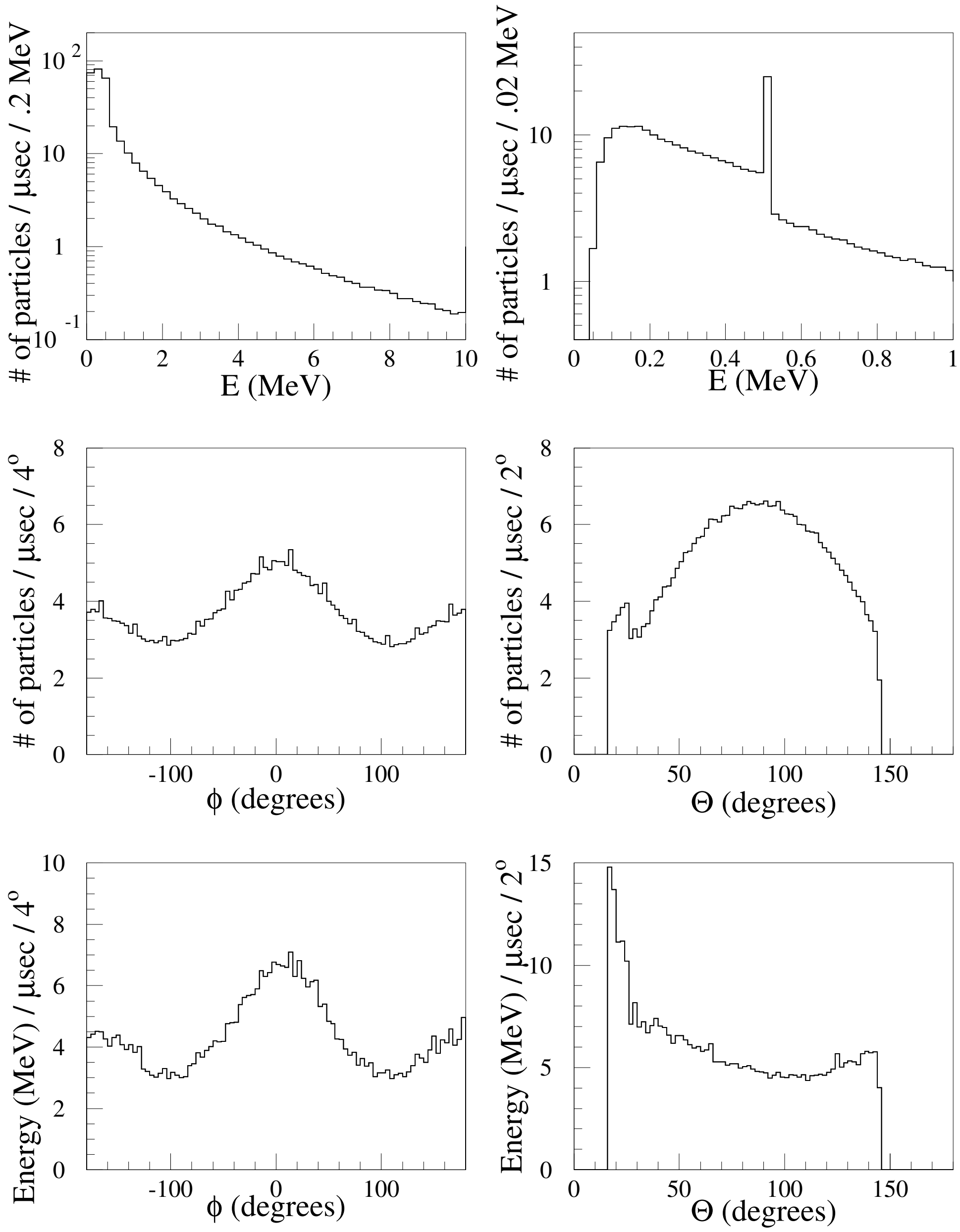

Figure 12-9. *Energy, azimuthal, and polar angle distributions of photons incident on the front face of the calorimeter. Also included are the angular distributions of energy flow. Rates correspond to number of incident particles and energy per* μs*.*

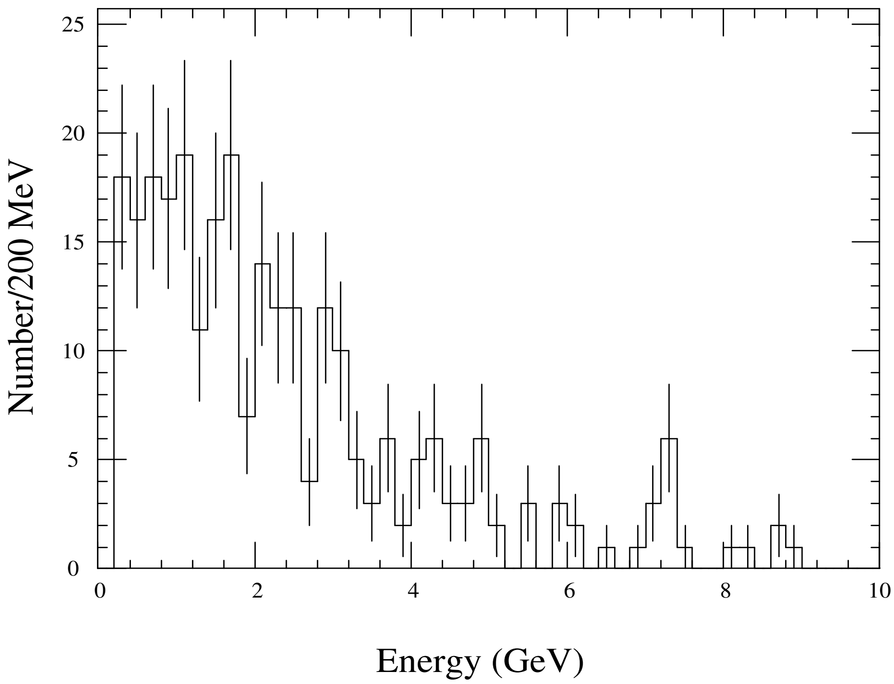

Figure 12-10. *The energy distribution of photons in electromagnetic showers which interacted hadronically, causing a charged track trigger.*

months. We are also actively investigating alternative models as a check of the current results.

At this stage in its development, it is difficult to evaluate the errors on GELHAD results. Using the model in which the photon is absorbed by a nucleus (model 1) at all energies instead of the model in which the photon is replaced by a pion (model 2) above 150 MeV results in a factor of 3 drop in the drift chamber trigger rate, while the calorimeter trigger rate remains virtually unchanged. The drop in the drift chamber trigger rate can be traced to a substantially lower pion multiplicity in model 1 compared to model 2. Only a program of comparison with data can establish the uncertainties and lead to an improved model.

12.3.4 Luminosity Backgrounds

Radiative Bhabhas

The radiative Bhabha process, $e^+e^- \to e^+e^-\gamma$, is a potentially large background because of its relatively large cross section. Outgoing degraded particles from the IP in each beam are

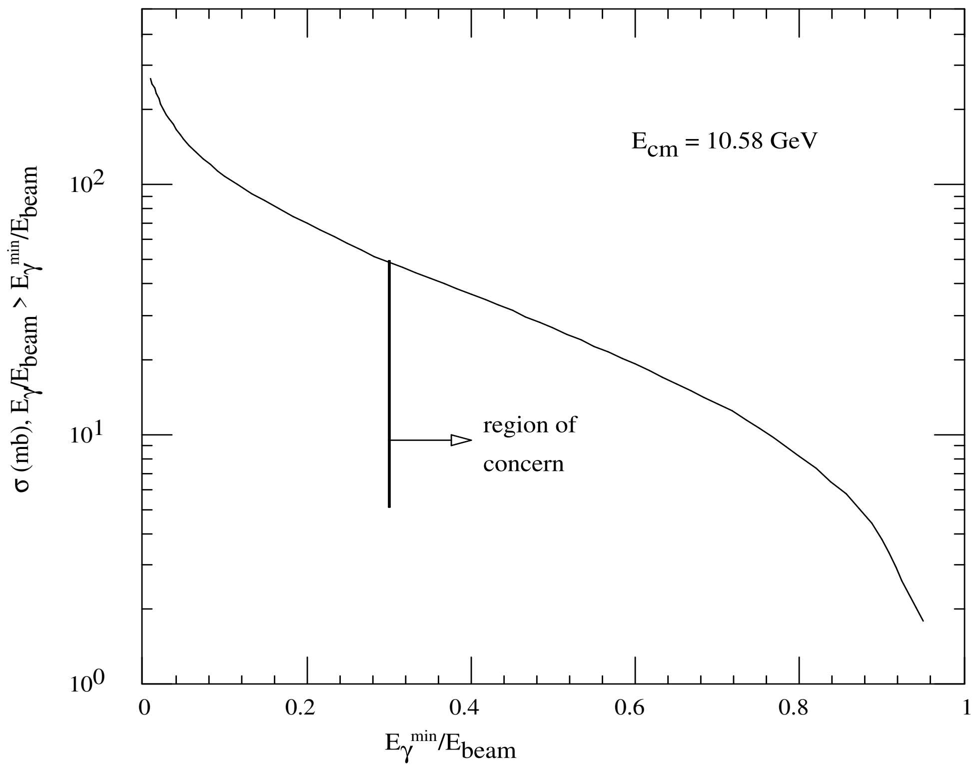

Figure 12-11. *Radiative Bhabha integral cross section versus minimum fractional photon energy.*

swept into the beam pipe by B1 and Q1. Figure 12-11 shows the radiative Bhabha cross section versus the minimum energy of the radiated photon that caused the degraded particle to hit the beam pipe, normalized to the beam energy.

To study the contribution of radiative Bhabhas to occupancy and radiation damage, we have used a Monte Carlo event generator called BBBREM, developed for LEP by Kleiss and Burkhardt [Kle94], and modified for an asymmetric collider. Individual events generated at the IP by BBBREM were input to OBJEGS and tracked until they hit beam line components and showered. Figure 12-12 shows the energy deposited per μsec in the beam pipe and other components (the peak at 240 cm is from radiative Bhabhas bent by B1 into the Q2 septum).

For particles that hit the beam pipe between the IP and the end of Q1 (*i.e.,* those less than 2.3 GeV), the rate from the LEB is about 5 times higher than that from the HEB due to the difference in cross section. However, in the HEB, there is an additional source from degraded electrons in the energy range 5.0–6.5 GeV that impinges on the Q2 septum at 2.4 m from the IP.

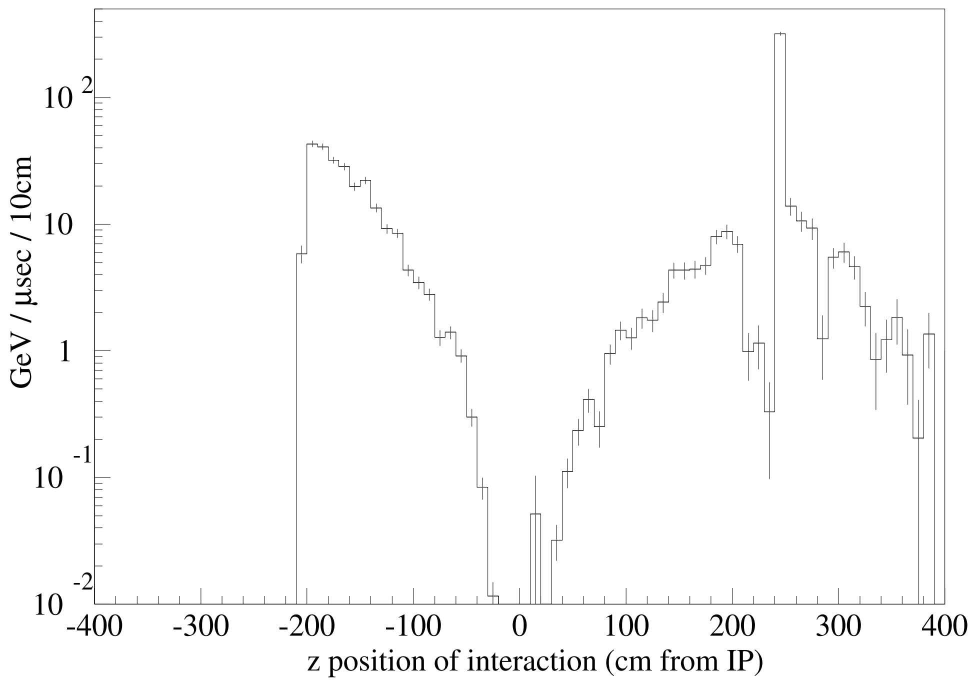

Figure 12-12. *Energy deposition from radiative Bhabhas versus distance from interaction point (in cm).*

Within ± 2.5 m of the IP, the power deposited by radiative Bhabhas is approximately two orders of magnitude more than the power from lost beam particles. Fortunately, the higher energy particles are hitting the beam pipe farther from the IP, and the resultant electromagnetic showers are mostly directed away from the vertex detector and central drift chamber.

To determine the effect of radiative Bhabhas on the detector, they were included in GEANT with lost particles from beam-gas bremsstrahlung and Coulomb scattering. With the addition of high-Z shielding around Q1 and the magnetic shielding around Q2, the rate of photons into the detector was found to be small compared to the lost particle contribution.

Elastic Bhabha Scattering

The cross section for elastic Bhabha scattering with angles large enough to cause the scattered particles to hit the beam pipe within Q1 is about four orders of magnitude smaller than the corresponding radiative Bhabha cross section. In terms of power lost within ± 2.5 m of the IP, elastic Bhabhas are at least two orders of magnitude lower than both radiative Bhabhas and lost particles. Therefore, we consider background from this process negligible.

Two Photon Reactions

We neglect this process, in which the e^+ and e^- both radiate in the same interaction, since its cross section is some 1000 times smaller than the radiative Bhabha process [Bai81], and the presence of two degraded beam particles arising from the same beam crossing does not give rise to any special background condition.

Landau-Lifshitz Pairs

In this process, an e^+e^- pair is produced at the IP, and a low-energy particle with fairly large transverse momentum may hit the Be beam pipe [Che91]. The magnetic shielding from the 1.5 T solenoid greatly reduces this background contribution to the point where it is negligible.

12.3.5 Other Sources

Beam-Gas Interactions at the IP

Electrons and positrons in the cores of the beams scatter off molecules inside the beam pipe near the interaction point, producing hadrons. This process does not include the more severe backgrounds due to lost-particle hadronic interactions. Rates of triggers were estimated using the electro-production code EPC [Lig88] interfaced to the detector GEANT simulation BBSIM.

The EPC generator program models the double-differential nucleon production cross section due to electrons scattering off thin targets of nuclei. The accuracy of the program is about 20% [Lig88]. Only single-particle cross sections are produced by the program. The EPC program was used to make tables of double-differential cross sections for each type of final-state hadron for beam electrons and positrons incident on a thin target of nitrogen molecules.

The single-particle final states p, n, π^0, π^+, and π^-, were generated and tracked by GEANT through the detector. The simulation was lacking in that two-particle states were not generated. The main contribution to true two-track final states is expected to be from $\Delta \rightarrow \mathrm{p}\pi$, which is the sole source of pions in the EPC program. To obtain a high upper limit of the two-track drift-chamber Level 1 trigger rate due to Δ decay, it was assumed that all protons that give rise to a track were accompanied by an A-track pion. (An A track is defined as a particle track which passes through all layers of the drift chamber, while a B track passes through only the inner half of the chamber.) That is, the upper limit to the two-track trigger rate was assumed to be the proton-induced B-track rate (including A tracks). A similar upper limit was estimated for the calorimetric trigger.

The estimated trigger rates due to beam-gas interactions near the interaction point [Kra94b] are given in Chapter 10. The upper bound for the total Level 1 rate was found to be comparable to the physics rate for a vacuum of 10 nTorr and thus is tolerable, with a large safety margin. The trigger rate due to beam-gas events would be significantly lowered by a trigger level that selects the track z position to be near the interaction point, such as a trigger using the vertex detector. The accuracy of the beam-gas trigger-rate calculation could be improved through the use of a program that provides final-state particle correlations.

Cosmic Rays

Cosmic rays are caused by high-energy particles interacting with the atmosphere, producing pions and kaons that decay into muons, and producing showers. At ground level, the majority of penetrating particles are muons.

Cosmic rays are important to *BaBar* in two ways: they cause about 500 Hz of Level 1 trigger rate when using a trigger line containing only a loose calorimeter definition, and they can be used to calibrate elements of the detector.

The cosmic-ray muon generator HEMICOSM [Bri94] was developed for study of trigger rates and for future study of the detailed flux incident on various detector components. The generator HEMICOSM was interfaced to BBSIM and used to study detector response. The program uses an accurate theoretical flux prediction that varies as a function of both momentum p and zenith angle [Dar84]. The ratio of μ^+ to μ^- was taken to be 1.25 [All84, PDG92].

There are reasonably accurate measurements of the flux incident on a unit horizontal area at sea level for hard muons, where a hard muon is defined to be one that penetrates 15 cm of lead, corresponding to a momentum slightly over 0.3 GeV/c. The measured value for the hard component of the flux, $0.013\,\mathrm{cm}^{-2}\,\mathrm{sec}^{-1}$ [PDG92], was used to calculate the incident muon rate.

The calculated trigger rates due to cosmic-ray muons [Kra94a] are given in Chapter 10. The rates for the theoretical momentum spectrum were found to agree to within 5% of those from a measured momentum spectrum [All84].

Muons from Collimators

There is a potential background from muons produced by lost beam particles on either side of the detector near the IP. For a single beam lifetime of 1.5 hours, the HEB(LEB) beam loss rate is $3.5 \times 10^3/\mu$s ($7.7 \times 10^3/\mu$s). Assuming this loss is due to beam-gas scattering and is uniform around the ring, the fraction lost by each beam within the 60 m straight section on either side of the IP is $60/2200 = 0.027$. For muon momenta above 1 GeV/c, the number of muons/electron [Tsa74] from full energy lost particles on copper in the HEB(LEB) is $5.0{\times}10^{-6}$ (2.9×10^{-7}), giving muon rates of $4.8 \times 10^{-4}\,\mu$s and $0.6 \times 10^{-4}\,\mu$s from the HEB and LEB, respectively. Making the conservative assumption that all the produced muons reach the detector, the combined rate is about 600 Hz.

Tunnel Shine

The detectors at PEP-I had shielding walls, ranging from one-fourth of an inch Pb to eight inches of steel rods, separating the IR hall from the tunnels on either side, to protect against various radiations present in the tunnels. No doubt *BaBar* will require similar protection. The forward end, facing the proton alcove, is fairly well-protected by the steel plates of the magnet endcap. The DIRC water tank on the other end may be more sensitive to radiation.

12.4 Background Rates and Detector Responses

This section describes the effects of machine-induced backgrounds on the various components of the *BaBar* detector, specifically the vertex detector, drift chamber, particle identification system, calorimeter, and muon detector. As shown below, all detector components can function with virtually no degradation in performance at the nominal background levels for ten years or more. It is desirable to maintain reasonably good performance and lifetime at background levels above this nominal level for a number of reasons. First, there are inherent uncertainties in the above predictions of background levels, both in the assumptions that go into the generation of the source and in simulating the detector response. Second, the accelerator running conditions may vary significantly, especially in the early stages when the machine is being tuned to the optimal operating point.

For most of the significant sources described above, there are not large uncertainties in the generated rates. The dominant contributor to occupancy and radiation damage effects is from the electromagnetic showers produced by lost beam particles hitting near the IP (Section 12.3.2). This source also produces significant contributions to the background trigger rate through the photoproduction of hadrons. As discussed in the section above on lost particles, a major uncertainty in this process is lack of knowledge of the final vacuum pressure distribution in the interaction region, though preliminary designs suggest that the uniform 1 nTorr is probably a safe assumption. The photoproduction model and its resulting impact on trigger rates remain uncertain, and work is in progress to check them against data and other models.

A major concern relating to machine operation is the radiation dose received during injection. High voltage will be lowered during injection for some detector components to protect them from harm. Components such as silicon detectors, readout electronics, and calorimeter crystals will still be sensitive to this added dose from injection. This is currently being studied in simulations. Experience at other e^+e^- machines suggests that the integrated radiation dose received from injection can be as large as that received from normal running conditions (*i.e.,* the total dose should be assumed to be at least twice the nominal level).

One purpose of this section is to describe the ability of each component to handle backgrounds above the nominal value. As the background increases, the effects vary from reduced efficiency or high occupancy in a small region of the detector, with little impact on overall detector performance, to actual device failures that occur at very high background levels and result in downtime to replace components.

12.4.1 Vertex Detector

Vertex Detector Overview

The silicon vertex detector is described in detail in Chapter 4. The essential details of the geometry and other features relevant to the background analysis will be summarized here.

The vertex detector has five layers of sensors surrounding the beam pipe. The three inner layers are a traditional barrel-style geometry with six detector modules per layer, each covering 60° in azimuth. The minimum radii of the layers are located at 3.2, 4.0, and 5.2 cm, respectively. The outer two layers are arch shaped, with tilted detectors in the forward and backward directions to minimize the total area of silicon and to avoid small track crossing angles. There are 16 detector modules in azimuth in Layer 4, and 18 in Layer 5. The barrel sections of Layers 4 and 5 are located at minimum radii of 12 and 14 cm, respectively.

Double-sided silicon strip detectors are employed with ϕ strips running parallel to the beam line and z strips oriented at 90° to the beam line. The vertex detector covers the solid angle over the region $17.2° < \theta < 150°$. The readout electronics are located outside of the active tracking volume in a 1 cm-thick space surrounding the B1 magnets.

Vertex Detector Backgrounds

The primary source of backgrounds in the vertex detector is lost beam particle interactions (Section 12.3.2). Synchrotron radiation is produced copiously near the IP but is carefully shielded so that very little reaches the vertex detector.

Beam-gas scattering produces off-energy electrons as well as photons. These lost particles can impact the vertex detector, where they have several effects. Radiation damage from the ionization they produce can degrade the performance of both the silicon sensors and the front-end readout electronics. The additional occupancy can result in inefficiency for hits from physics-related tracks and pose bandwidth problems for the DAQ system. Offline, background hits can confuse the pattern recognition algorithms. These effects have all been studied, and the results are summarized here.

Radiation Damage

The BBSIM detector simulation package is used to determine the flux of ionizing radiation through the silicon from lost beam particle showers. In units of kradper operational year, *i.e.*, 10^7 s, Layer 1 sees an average of about 33 krad/yr, Layer 2 sees 19 krad/yr and Layer 3 sees about 6 krad/yr [Cou95]. The dose is not uniformly distributed, as shown in Figure 12-13. There are sharp peaks in the bend planes of the machine at $\phi = 0, \pi$. This results in a highly nonuniform dose per stave in the inner layers. The worst case is in Layer 1, Stave 1, where the average yearly dose is 82 krad/yr, and the peak dose is 240 krad/yr over a region covering approximately 6° in azimuth.

This radiation will result in increased leakage current. Experimental measurements of the effects of ionizing radiation on silicon detectors have shown an increase in the leakage current of approximately 0.7 nA/cm^2/krad for detectors similar in design to those planned for *BaBar* [Joh09]. The vertex detector should withstand 10 times the yearly dose in order to have a reasonable safety factor over the estimated two-year period between access for repairs. There may be additional radiation damage caused during periods of non-optimal machine conditions, such as during injection or machine tuning; such effects have been known to increase the integrated radiation dose by a factor of 2 over the nominal calculated level. By designing the vertex detector to withstand 10 times the yearly dose, we account for this additional dose, integrated over a period of two years, with some additional margin for safety.

For Layer 1, Stave 1, 10 times the average yearly dose results in an estimated increase in leakage current of approximately 26 nA per strip in both ϕ and z. The corresponding noise is 166 e^- in equivalent noise charge (ENC), which must be added in quadrature to the ENC of the input amplifier; the latter ranges from about 400 e^- for the z strips to a little over 600 e^- for the ϕ strips. The resulting increase in noise is less than 8% in both cases. In the worst azimuthal region, the increase is about 72 nA per strip resulting in an ENC of 260 e^-, but this affects only the ϕ strips. Adding this noise in quadrature with the noise of the input device results in an increase of about 9% in the total ENC.

The front-end readout ICs are located just outside of the active tracking volume and are mounted on hybrids supported from cones which surround the B1 magnets located on either

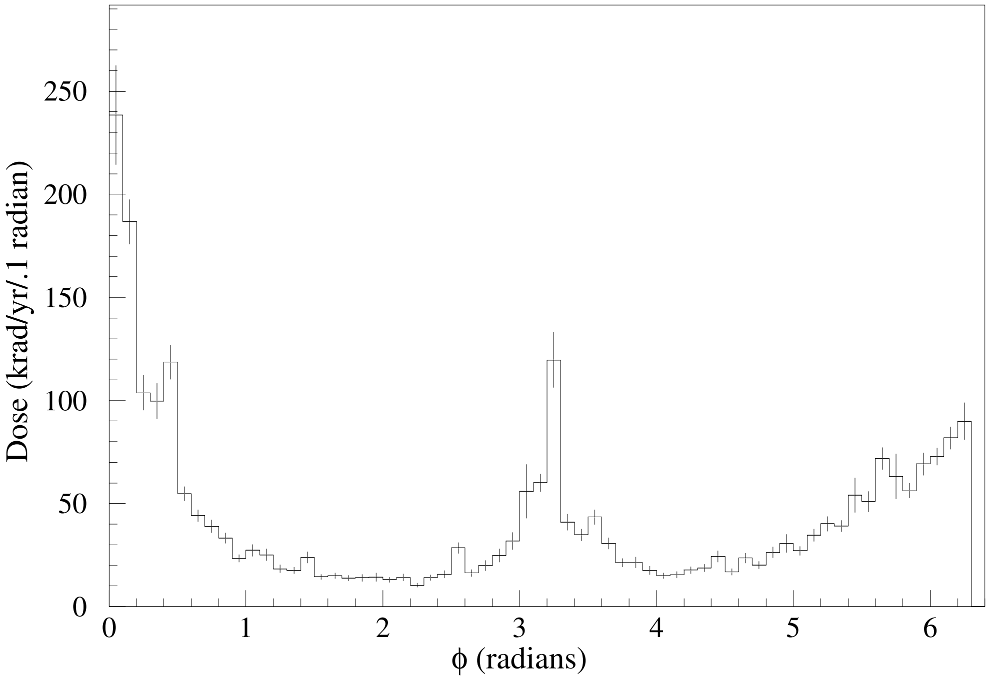

Figure 12-13. *Dose as a function of ϕ in vertex detector Layer 1, measured in krad/10^7 sec/0.1 radian.*

side of the IP. Flexible circuits connect the silicon detector strips to the readout ICs, so they are not constrained to be at the exact radius of the detectors. In the inner layers, the ICs are located at a slightly larger radius than the detectors they service. The readout ICs for Layer 1 are located at approximately the same radius as the detectors for Layer 2, so we can use the Layer 2 radiation levels for the Layer 1 readout ICs. The worst case in Layer 2 is Stave 1, which receives an average dose of 47 krad/yr with a peak value of 110 krad/yr.

The readout ICs must tolerate 10 times the maximum expected dose; this requirement implies the use of radiation-hard circuits. For the planned CMOS technology, a radiation-hard process is available from several vendors. For the baseline design, the Honeywell process has been chosen because it is offered with a 0.8 μm feature size with three metal layers; these options are desirable to optimize the IC layout and minimize the IC dimensions. The noise characteristics of the Honeywell process have been studied before and after irradiation. A slight increase in noise relative to the non-radiation-hard HP CMOS process is observed before irradiation, on the order of 20% at 3 MHz, which is the frequency of interest for the risetimes used in the inner layers. After irradiation to 500 krad, the noise increases by 15% at 3 MHz; after 1.5 Mrad the increase is 30%.

Stave	Layer 1 z	Layer 1 ϕ	Layer 2 z	Layer 2 ϕ
1	3.1%	1.4%	2.1%	1.3%
2	1.1%	0.6%	0.8%	0.5%
3	0.4%	0.3%	0.2%	0.3%
4	1.3%	0.6%	0.8%	0.5%
5	0.6%	0.4%	0.4%	0.3%
6	1.1%	0.6%	0.7%	0.5%

Table 12-3. *Occupancy in Layers 1 and 2 at nominal background.*

Background Occupancies

The percent occupancy in a one μs window versus stave number for Layers 1 and 2 is shown in Table 12-3 [Cou95]. The distribution is peaked in a manner similar to the radiation damage, with significantly higher occupancy in Staves 1 and 4.

The background occupancy is fairly high, and this has some important consequences for the readout architecture. One notable consequence is that a data-push readout is not feasible due to the large data transmission bandwidth that would be required; this in turn implies a fast Level 1 trigger to enable the vertex detector readout [Lev94a]. The Level 1 trigger is described in Chapter 10; it will have a latency of no more than 10 μs and an uncertainty of no more than 1 μs.

The vertex detector readout system must be able to cope with up to 10 times the nominal background occupancy. The safety factor of 10 is taken into account for occasional increases in occupancy that may occur during non-optimal periods of running. This requirement is met by providing sufficient bandwidth in the data transmission system, together with enough buffers in the readout section of the front-end chip to even out the fluctuations in rate.

The worst case is again Layer 1, Stave 1, where the occupancy at 10 times nominal background is 30% for the z strips. Each stave will have four data links, two on each end, to independently transmit data from the ϕ and z strips, and each data link is expected to have a transmission rate of at least 60 Mbits/s. At the maximum Level 1 trigger rate of 2 kHz, assuming 16 bits/hit plus a per-chip overhead of 16 bits, the total bandwidth out of the Layer 1, Stave 1 z strips is about 6 Mbits/s per half detector module. The deadtime fraction for 10 times nominal background, under these assumed conditions, is plotted versus trigger rate in Figure 12-14 for one, two, three, and four back-end buffers [Lev94b]. For three buffers at the expected maximum Level 1 trigger rate of 2 kHz, the deadtime is about 1% and exhibits linear behavior.

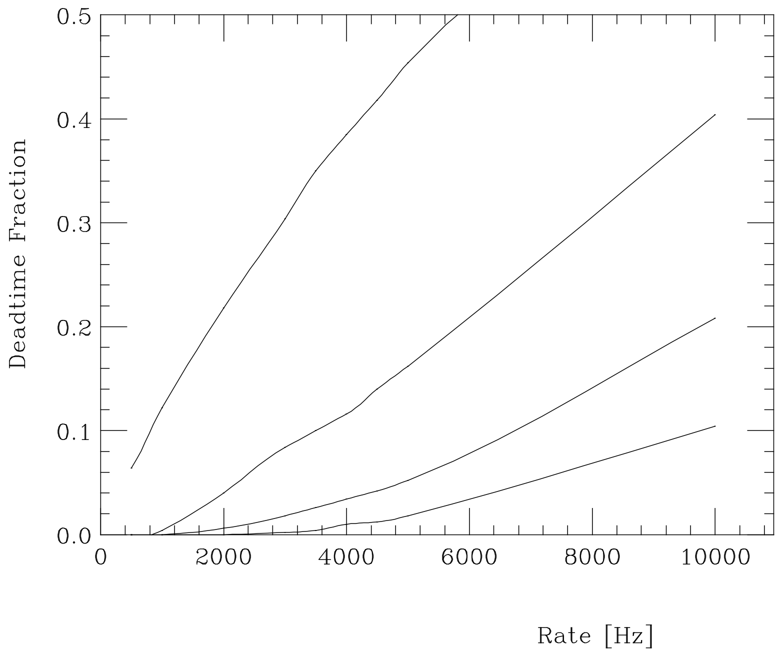

Figure 12-14. *Deadtime fraction for 10 times nominal background vs. trigger rate for one, two, three, and four back-end buffers.*

Pattern Recognition

The offline pattern recognition capabilities of the vertex detector have been studied using a detailed GEANT simulation, together with a Kalman filter track finding algorithm. The study assumed that tracks which generated at least ten hits in the drift chamber would be found by the drift chamber and extrapolated into the vertex detector. Tracks with a p_t below 90 MeV/c which fail this criteria are found using the vertex detector for stand-alone pattern recognition. The overall pattern recognition efficiency is found to be very high, approaching 100%, for generic B decays with nominal and with 10-times-nominal backgrounds superimposed (see Chapter 4). The fake rate, defined as the number of found tracks per event which have fewer than half of their hits from a real track, is seen to go up as background levels increase. Most fake tracks have a p_t below 90 MeV/c and are due to random combinations of background hits in the vertex detector alone. However, the five layers of the vertex detector provide a powerful pattern recognition capability, and the fake rate can be kept to an acceptable level (fewer than 0.05 fake tracks/event) even at 10 times the nominal background.

12.4.2 Drift Chamber

Wire aging and chamber occupancy due to beam-related backgrounds are two issues of concern for the operation of wire chambers. Aging refers to changes in gain or increases in noise due to material deposited on the wires from the gas-avalanche process. Chamber occupancy is the fraction of cells that contain random hits during the event resolving time, *i.e.,* the full drift time. If the occupancy exceeds a few percent, pattern recognition becomes difficult.

The design of the BaBar drift chamber has been guided by the desire to minimize the amount of material in the chamber, thus permitting the best possible measurement of the relatively low momentum tracks necessary for the *CP* asymmetry studies. The drift chamber is 280 cm in length and occupies the radial space between 22.5 cm and 80 cm, providing a polar angle acceptance down to 300 mr. It is bounded by the support tube at its inner radius and the particle identification device at its outer radius. The chamber contains approximately 40 layers of wires arranged in a small-cell geometry, with a total of about 7000 sense wires and 45,000 field wires. The sense wires are 20 μm-diameter gold-plated tungsten and the field wires are 55 μm-diameter gold-plated aluminum. The chamber is filled with a helium-based gas that, along with the choice of aluminum wire, represents a minimal number of radiation lengths. The gas alone has a radiation length of $\sim$800 m. The 40 layers of individual sense and field wires correspond to 0.02% and 0.08% of a radiation length, respectively, for normal incidence.

The chamber endplates and the inner and outer cylinder walls are also being designed using low-mass materials. The endplates are foreseen to be made of carbon fiber, corresponding to less than $0.03X_0$. The inner cylinder wall's function is to provide a gas seal and will be made of carbon fiber or beryllium, representing $\lesssim 0.002X_0$, while the outer wall, which supports the wire load, will be of aluminum or carbon fiber, giving $\sim 0.03X_0$.

Beam-related backgrounds which occur during beam injection are not a problem for the drift chamber, for which the voltage can and will be turned off. The expected backgrounds in the drift chamber have been calculated for a 1 nTorr beam vacuum. The drift chamber occupancies for a resolving time of 1 μs, which corresponds to the maximal drift time, are shown for each layer in Figure 12-15. The distribution is peaked at the innermost layer, where occupancies of 0.5% are expected. For the outer layers, the occupancies are $\sim$0.03%. These results, based on a chamber with a radiation length of 800 m, do not include conversions in or scattering by the wires. A simple method of estimating an upper limit on the effect of the wires on the occupancies would be to smear the wire material over the chamber volume, resulting in a radiation length of 400 m, which would roughly double the occupancies. More realistically, the effect of the wires would increase the occupancies in the outer layers, while leaving the results for the innermost layers unchanged.

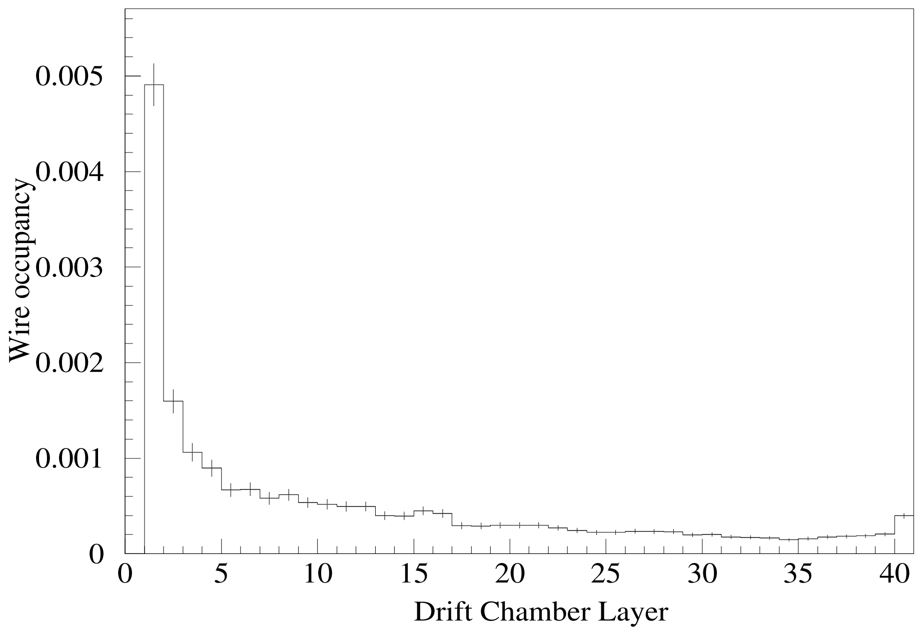

Figure 12-15. *Expected background occupancies for each drift chamber layer due to converted photons from showers produced by lost particle interactions.*

The occupancies have been calculated without including the effects of signal crosstalk, expected to be ∼1–3%. Since most background events would produce low-momentum tracks which spiral in z within a few cells (depending upon the wire orientations), producing very large signal pulses, the number of neighboring cells which also contain pulses due to electronic crosstalk could be sizable.

In general, chamber occupancies of a few percent are tolerable but render the problem of pattern recognition and segment-finding more difficult. Occupancies which approach or exceed ∼10% make track finding almost impossible.

For a uniform distribution along the wires, the energy deposition on a wire corresponds to an integrated charge of $0.001\,\mathrm{C/cm}/10^7$sec for the innermost drift chamber layer. The charge deposition in the drift chamber is not uniform, showing factors of 2 variation in ϕ and z. Taking these factors into account, the expected integrated charge for some regions of the inner layers could be as high as $0.005\,\mathrm{C/cm}/10^7\,\mathrm{s}$ for the 1 nTorr beam vacuum.

Significant amounts of charge accumulated on the sense wires can lead over time to deposits on the wires, resulting in electrical discharges and current draw. A conservative limit on the integrated charge on a wire which can be safely tolerated is 0.1 C/cm. This limit can be extended depending upon the ionizing gas mixture. For example, small amounts of

	Bars	Tank
# of Charged Particles	16	0.7
# of Hits	32	8.0

Table 12-4. *Mean number of charged particles crossing the DIRC per μs due to beam lost secondaries.*

H_20 [Kad91] and CF_4 [Ope91] in combination with ionizing gases have been shown to extend this limit to $\gtrsim$1.0 C/cm.

12.4.3 Particle ID

The particle identification system described in Chapter 6 consists of a ring-imaging Cherenkov system (DIRC) covering the barrel region and an aerogel threshold counter in the forward direction. The DIRC consists of quartz bars read out with phototubes mounted on a water tank in the backward ($-z$) direction.

The background level in the aerogel detector has not been studied in detail. The principal source of background is likely to be the flux of low-energy photons from lost particle showers. Backgrounds from conversions of these photons in the aerogel itself are expected to be small due to its very low density. The contribution from the support structure and photodetectors are currently under study.

Several background sources might affect the DIRC's performance: event related backgrounds, synchrotron radiation photons, beam-gas interactions, cosmic rays, phototube dark noise, etc. The program BBSIM has been used to simulate the detector response. Each random background source has been integrated over an assumed 50 ns readout time.

Lost Particle Backgrounds. The background induced in the DIRC from lost beam particles has been estimated as described in Section 12.3.2 with the assumption of a uniform beam line pressure of 1 nTorr. The mean number of charged particles crossing the quartz bars and the water tank every μs and the number of hits produced at the nominal background rate are listed in Table 12-4. These numbers are to be compared to an average of 345 hits for a typical physics event in a 50 ns window. The deduced mean rates expected per PMT and per readout time at 10 times nominal background are around 20 kHz for a uniform beam line pressure of 1 nTorr.

Radiative Bhabha. The radiative Bhabha process, $e^+e^- \rightarrow e^+e^-\gamma$ is a potentially important source of background. A BBSIM simulation of this process predicts that about 25 charged particles per μs from secondary interactions crossing the DIRC, yielding an average of 75 hits, 40% due to Cherenkov emission in the bar, 60% in the tank. The background from radiative Bhabhas is on the same order of magnitude as the nominal background from lost particle interactions. The showers from radiative Bhabhas tend to originate from around Q1 and Q2, suggesting the possibility of additional shielding to reduce this background.

Other external backgrounds such as synchrotron radiation and cosmic rays have very small or negligible impact on the DIRC response (see Chapter 6).

12.4.4 Calorimeter

The main background in the CsI calorimeter is low-energy photons from lost beam particle showers. Energy and angular distributions for these photons are shown in Figure 12-9 for the nominal background level. About 330 photons per μs, with a total energy of 0.39 GeV, are incident on the calorimeter. The median photon energy is $\sim$500 keV, and about one photon per μs is above 20 MeV. Major background-related issues for the calorimeter are radiation damage, energy resolution degradation, creation of extra showers in events, and trigger rates.

The radiation dose was estimated by assuming that the photons of Figure 12-9 are absorbed in the first 2 cm (9 g/cm^2) of the calorimeter. At nominal background, the radiation dose for 10^7 s/yr running is about 45 rad/yr at $\theta = 90°$ and 90 rad/yr at $\theta = 300$ mr. Larger doses are expected from injection and machine studies, based on the experience of existing storage ring operation. Scaling typical CESR operations to the PEP-II design beam currents gives a radiation dose of about 1.5 krad/yr at a radius of 45 cm, and 0.5 krad/yr at 100 cm [Blu86]. Both are well within the tolerable dose rate of 10 krad/yr.

The effect of backgrounds on photon energy resolution was studied using lost beam particles generated by TURTLE as input to BBSIM, where they were showered in the same events as the photons of interest. Backgrounds corresponding to nominal and 10 times nominal levels in 1 μs windows were generated together with 100 MeV photons in the barrel and forward endcap. Comparison of the resolutions with the zero background case, for which $\sigma = \mathrm{FWHM}/2.36 = 1.8$ MeV, shows contributions, in quadrature, of 0.55 MeV from nominal background and 1.05 MeV from 10 times nominal background.

A small fraction of the photons from beam backgrounds has sufficient energy to be detected as extra photons in physics events. Efficient B-meson reconstruction requires measurement of photon energies as low as 20 MeV. The rate of photons with energies above 20 MeV from lost beam particles is 0.7 per μs in the barrel and 0.4 per μs in the forward endcap at nominal background. Timing information from the shaped calorimeter signals may be used to discriminate between photons which belong to events and out-of-time background photons.

Some beam background particles reaching the calorimeter have sufficient energy to contribute to the trigger rate. Work is in progress to estimate this rate reliably and to improve the design of detector shielding if necessary. Section 10.8 contains further discussion of this issue.

12.4.5 Muons

The Instrumented Flux Return (IFR) is well shielded from potential background sources by the calorimeter, magnet, and flux return steel. Only the endcap chambers are close to the beam line, and these are protected by flux return and magnetic shielding for the beam line quadrupoles. Backgrounds from the previously discussed sources and from the irreducible cosmic ray flux are expected to be small. The outermost layer of the IFR may be sensitive to soft electromagnetic backgrounds in the detector hall originating from the PEP-II arcs. Shielding walls in the tunnel mouths will be necessary to isolate the detector from the arc radiation sources.

12.5 Physics Impact

The impact of backgrounds on the various detector components ultimately must be evaluated in terms of their effect on the overall physics goals of *BaBar*. Two requirements can be compromised by high background levels: trigger selection and data acquisition for events of interest; and offline reconstruction of the data.

As described above, a principal source of background trigger rates is the photoproduction of hadrons in the showers initiated by lost particles, contributing to both a charged-track trigger in the central drift chamber and to a calorimeter energy trigger. The rate is acceptable at nominal background levels but begins to saturate the Level 1 trigger rate at around 10 times nominal. Chapter 10 describes in detail the design of the trigger and steps taken to deal with the possibility of a high trigger rate from this source. The conclusion of this discussion is that some flexibility is required in the trigger to allow the energy and momentum thresholds to be raised if the rate from this source becomes too high. The loss of trigger rate for some events of interest from the higher thresholds is also discussed in this chapter.

The effect of backgrounds on event reconstruction within a particular detector component has been studied in several cases, including, for example, track reconstruction in the silicon vertex detector and the degradation of calorimeter resolution at above nominal background levels. These are examples of two major effects of backgrounds on offline event reconstruction:

the inability to accurately reconstruct events due to inefficiency and/or the confusion caused by the high occupancy, and the degradation in resolution from the overlap of hits from background and the physics event. The vertex detector shows a clear ability to maintain good reconstruction efficiency at 10 or more times nominal levels, due largely to its fine sampling and the redundancy of a five-layer detector. Similar studies with the drift chamber are in progress. Again the large number of layers (40) and low occupancy are expected to offer robust track reconstruction at above-nominal background levels. At 10 times nominal background the flux of photons noticeably degrades the calorimeter resolution only for photon energies below 50–70 MeV. This effect will be seen as a small worsening of the reconstructed mass resolution for generic B decays with a π^0 in the final state but will not effect modes with higher momentum π^0s (*e.g.,* $B \to \pi^0\pi^0$).

A real assessment of the effect of backgrounds on overall event reconstruction awaits the development of the reconstruction algorithms, a major effort that is in progress but not complete.

12.6 Summary

Extensive work has been done by the *BaBar* collaboration to develop the tools to predict the background rates in PEP-II and their effects on the various detector components. Work continues on refining these estimates and checking the results with data where available. There is also interaction with the PEP-II designers regarding aspects that affect background rates, *e.g.,* the degree of vacuum pumping in the interaction region. The principal aim in these studies is to ensure that the *BaBar* detector physics goals are not compromised by machine-induced backgrounds. The detector design performance can be degraded due to high occupancy causing inefficiencies, deadtime, or pile-up effects, and radiation damage, causing impaired performance or frequent downtime to replace components. Some safety margin (generally taken to be a factor of 10) is required to account for uncertainties in the calculations, the assumed PEP-II running conditions, and in the case of radiation damage, the dose accumulated during injection and machine studies. As explained in Section 12.1.4, the design of the injection system for PEP-II suggests that injection will be cleaner than for other machines. Nevertheless, the working assumption in the *BaBar* detector design is that the dose from injection will equal that of normal running (in the case of the calorimeter, a direct scaling of CLEO results is used).

Table 12-5 summarizes the contribution to occupancy from the dominant lost particle background for the more sensitive elements of the *BaBar* detector. Careful masking design and shielding around the beam line components has reduced the contribution from synchrotron radiation and radiative Bhabhas to a low level. Also in Table 12-5 is an estimate of the limit on how high a value could be tolerated without compromising the performance goals of

	Silicon Layer 1		Drift Chamber		Particle ID	Calorimeter
	Average	Stave 1	Average	Layer 1	(DIRC)	Photons
Occupancy	1.3%	3.0%	0.05%	0.5%	0.015%	$1.1/\mu s$
Limit	20%	20%	10%	10%	2%	$10/\mu s$
Safety	15	6	200	20	130	9

Table 12-5. *Occupancy in various detector components of BaBar. Calorimeter entries are for photon energies above 20 MeV.*

	Silicon Layer 1		Drift Chamber		Calorimeter
	Average	Stave 1	Average	Layer 1	
Dose/10^7sec	33 krad	82 krad	0.0004 C/cm	0.0045 C/cm	1.5 krad
Limit	1500 krad	1500 krad	0.1 C/cm	0.1 C/cm	100 krad
Safety	45	18	250	22	67

Table 12-6. *Radiation dose in various detector components of BaBar.*

BaBar; the bottom row gives the resulting safety margin. The silicon detector has the lowest safety factors. The 20% limit on occupancy in this detector is set by the desire to maintain 90% or better hit detection efficiency. The worst stave of Layer 1 of the vertex detector has a safety margin below 10, but a larger loss in efficiency in this limited region of a single layer is not considered a serious compromise of its overall performance.

Table 12-6 gives the radiation doses in appropriate units for the detector. The first row gives the yearly dose, and the second row gives an estimate of the limit at which the performance begins to significantly degrade. The safety margin then determines the lifetime of the detector at nominal background levels. Included in this safety margin, though, must be some accounting for uncertainties in the calculated background levels and, particularly for the silicon and the calorimeter, the additional doses likely to be delivered to these systems during injection. The drift chamber will be ramped down in voltage during injection. The BaBar detector is expected to be operating for 10–15 years, but it is reasonable to assume that limited parts of the detector (such as sections of Layer 1 of the vertex detector or the forward calorimeter) could be replaced at intervals of three to five years. As noted in Section 12.4.1, small ϕ regions of Layer 1 of the silicon vertex detector will see higher doses (240 krad). These regions will have degraded signal-to-noise due to increased leakage current, but the small extent of the damage will not seriously affect the overall performance. The conservative approach of scaling the CLEO results on dose from injection is used for the calorimeter dose.

References

[All84] O.C. Allkofer and P.K.F. Grieder, "Cosmic Rays on Earth," Physik Daten 25–1, Karlsruhe, Germany, 1984.

[Blu86] E. Blucher *et al., Nucl. Instr. Methods* **A249**, 201 (1986).

[Bai81] V.N. Baier, V.S. Fadin, V.A. Khoze, and E.A. Kuraev, "Inelastic Processes in Quantum Electrodynamics at High Energies," *Phys. Repts.* **78**, 293 (1981).

[Bri94] M. Bringle, "Cosmic Ray Muon Monte Carlo Generator using the Hemisphere Method," *BaBar Note* # 163 (1994).

[Car91] D.C. Carey, K.L. Brown, and F.C. Iselin, "Decay TURTLE (Trace Unlimited Rays Through Lumped Elements): A Computer Program for Simulating Charged Particle Beam Transport Systems, Including Decay Calculations," SLAC–246 (1980).

[Che91] P. Chen, T. Tauchi, and D.V. Schroeder, "Pair Creation at Large Inherent Angles," in *Linear Collider IR and Final Focus Introduction,* edited by J. Irwin and D. Burke, SLAC–PUB–5652 (1991); also in Proceedings of the 1990 DPF Summer Study (Snowmass, Colorado), pp. 751–756 (1990).

[Cou95] D. Coupal, "Lost Particle Backgrounds in *BaBar*," *BaBar Note* # 210 (1995).

[Dar84] A. Dar, "Cosmic Ray Muons at Ground Level and Deep Underground," TECHNION–PHYS–84–41, Israel Institute of Technology, Haifa (1984).

[Deg94] P.V. Degtyarenko *et al., Phys. Rev.* **C50**, 541 (1994).

[Fes85] H.C. Fesefeldt, "The Simulation of Hadronic Showers, Physics, and Applications," Technical Report PITHA 85–02 (1985).

[GEA94] GEANT Detector Description Tool, version 3.21, CERN Program Library W5103, CERN (1994).

[Hal81] K. Halbach, "Design of Permanent Multipole Magnets with Oriented Rare Earth Cobalt Material," *Nucl. Instr. Methods* **169**, 1 (1980).

[Her87a] S.W. Herb, "Construction of Large Permanent Magnet Quadrupoles," CLNS–87/61 (1987).

[Her87b] S.W. Herb and J. Kirchgessner, "Operation of CESR with Permanent Magnet Interaction Region Quadrupoles," CLNS–87/64 (1987).

[Hea91] C. Hearty, "OBJEGS Users' Manual," *BaBar Note* # 73, (1991).

[Joh09] R. Johnson, "Radiation Damage Measurements on ALEPH Double-Sided Silicon Strip Test Structures," ALEPH Note 94–009 (1994).

[Kad91] J. Kadyk, *Nucl. Instr. Methods* **A436**, (1991).
J. Va'vra, SLAC–PUB–5207 (1990).
M. Danilov *et al., Nucl. Instr. Methods* **A274**, (1989).

[Kle94] R. Kleis and H. Burkhardt, NIKHEF–H/94–01 (1994).

[Kra94a] F. Kral, "Trigger Rates due to Cosmic Ray Muons," *BaBar Note* # 164 (1994).

[Kra94b] F. Kral, "Simulation of Trigger Rates due to Beam-Gas Backgrounds," *BaBar Note* # 165 (1994).

[Lev94a] M. Levi, "Impact of Backgrounds on the Silicon Vertex Detector Architecture and Detector Trigger," *BaBar Note* # 136 (1994).

[Lev94b] M. Levi, "A Simulation of the Vertex Detector Readout Buffers Using the Machine Induced Occupancy," *BaBar Note* # 193 (1994).

[Lig88] J.W. Lightbody, Jr. and J.S. O'Connell, "Modeling Single Arm Electron Scattering and Nucleon Production from Nuclei by GeV Electrons," Computers in Physics, May–June 1988, 57–64.

[Nel85] W. Nelson, H. Hirayama, and D. Rogers, "The EGS4 Code System," SLAC–PUB–265 (1985).

[Ope91] R. Openshaw *et al., Nucl. Instr. Methods* **A**, 298 (1991).

[PDG92] Review of Particle Properties, Particle Data Group, *Phys. Rev.* **D45** (1992).

[PEP93] "PEP-II, An Asymmetric *B* Factory: Conceptual Design Report," LBL–PUB–5379, SLAC–PUB–418, CALT–68–1869, UCRL–ID–114055, UC–IIRPA–93–01 (1993).

[Sny94] A. Snyder, "Electroproduction Triggers in *BaBar*," *BaBar Note* # 180 (1994).

[Tsa74] Y.S. Tsai, *Rev. Mod. Phys.* **46**, 815 (1974).